# Measuring Area-Averaged Vertical Motions with Dropsondes

Sandrine Bony, Bjorn Stevens

▶ **To cite this version:**

# Measuring Area-Averaged Vertical Motions with Dropsondes

SANDRINE BONY

*Sorbonne University, LMD/IPSL, CNRS, Paris, France*

BJORN STEVENS

*Max Planck Institute for Meteorology, Hamburg, Germany*

## ABSTRACT

Measurements of vertical profiles of areal-mean mass divergence, vorticity, and vertical velocity, based on dropsondes distributed over an area of $25\,000\,\mathrm{km}^2$, are presented. The dropsondes were released with high frequency along circular flight patterns during an airborne field campaign taking place over the tropical Atlantic near Barbados. Vertical profiles of the area-averaged mass divergence and vorticity were computed from the horizontal wind profiles, and the area-averaged vertical velocity was then inferred from the divergence. The consistency of measurements over pairs of circles flown within the same air mass demonstrated the reproducibility of the measurements, and showed that they characterize the environmental conditions on the scale of the measurement, rather than being dominated by measurement error or small-scale wind variability. The estimates from dropsondes were found to be consistent with the observed cloud field, with Lagrangian estimates of the mean vertical velocity inferred from the free-tropospheric humidity field, and with the mean vertical velocity derived from simulations using an atmospheric model representing kilometer-scale motions and initialized with meteorological analyses. In trade wind–like conditions, the divergence and vorticity profiles exhibit a rich vertical structure and a significant variability in space and time. Yet a few features appear to be robust, such as the presence of layers of mass convergence at the top of moist layers, extrema of the area-averaged vertical velocity at the top of the subcloud layer and in the midtroposphere, and minima around the trade inversion near 2 km. The analysis of spatial and temporal autocorrelation scales suggests that the divergent mass field measured from dropsondes is representative of the environment of shallow clouds.

## 1. Introduction

In Earth's atmosphere—on scales much larger than the depth (15 km) of the troposphere, which we call large scale—the magnitude of the mean vertical motion is only a hundredth of that of horizontal motions (a few centimeters per second vs a few meters per second). Yet large-scale vertical motions largely control the distribution of atmospheric water and trace substances (Newell 1963) and thus exert a disproportionate influence on weather and climate. Areas of large-scale ascent are associated with low pressure systems and an ensemble of updrafts occurring within narrow cumulus clouds surrounded by clear subsiding air, while areas of large-scale descent are associated with anticyclones, dry air in the free troposphere, and high static stability. More generally, the distribution and strength of large-scale vertical motions are closely associated with the heat and moisture budgets of the atmosphere (Yanai et al. 1973) and the regional distributions of cloud types, water vapor, and precipitation. Consistently, when running idealized simulations of the atmosphere with large-eddy simulation (LES) models, cloud-resolving models, or single-column versions of general circulation models, the specification of the mean vertical motion has emerged as one of the most influential components of the model forcing (Albrecht et al. 1979; Sobel and Bretherton 2000; van der Dussen et al. 2016), for which theoretical prescriptions (e.g., Sobel and Bretherton 2000; Romps 2012) are unconstrained by measurements.

ᵃ Denotes content that is immediately available upon publication as open access.

Indeed, measuring large-scale vertical motions in the atmosphere remains one of the greatest long-standing observational challenges of atmospheric science. In 1949 already, a meeting of the Royal Meteorological Society was emphasizing the importance and the commensurate difficulty of measuring directly, or inferring indirectly, large-scale vertical velocities on the order of a few centimeters per second (Bannon 1949). In the 1970s, several field programs, such as the Atlantic Expedition of 1965 (Augstein et al. 1973), the Atlantic Trade-Wind Experiment of 1969 (ATEX; Augstein et al. 1974), and the Barbados Oceanographic and Meteorological Experiment (BOMEX; Holland 1970; Holland and Rasmusson 1973), were designed to study specific cloud regimes, and they put the measurement of large-scale budgets of heat and moisture at their focus. For this purpose, these observational programs designed a network or large-scale array of stations or ships from which rawinsondes (or now radiosondes) could be launched simultaneously. The vertical profile of the mean mass divergence over the array could be inferred from the ensemble of soundings, and by using the equation of continuity, the mean vertical motion at each vertical level was deduced from the divergence of the horizontal wind. In some rare cases, such as during BOMEX (Holland and Rasmusson 1973), the mass divergence estimated from soundings could be compared at individual vertical levels with estimates derived from the horizontal wind measurements made on board an aircraft flying around the same domain.

For several decades, divergence measurements have derived from ship-based sounding arrays, with linear dimensions typically larger than 500 km. Nowadays, increasing interest in how clouds couple to circulation on scales of 20–200 km motivates interest in divergence over smaller areas, with linear dimensions more on the order of 100 km (Bony et al. 2017). These more intermediate scales are what Orlanski (1975) called the meso-$\beta$ scale. They are large, as compared to the scale of convection that reaches a depth of only a few kilometers, and are more commensurate with the scales over which the organization of shallow convection occurs, the typical grid mesh area of climate models in which convection is parameterized, and domain sizes over which it is becoming practical for large-eddy simulation studies. But because the methods we develop are also applicable to an understanding of measurements on these and yet larger scales, in this manuscript we adopt the term "large scale" to refer to scales of 50–500 km, as it is this range of scales to which our arguments are applied.

Lenschow et al. (1999, 2007) showed that the large-scale mass divergence at the top of the planetary boundary layer (PBL) could be estimated using wind measurements from an aircraft gust probe. These measurements were made in perhaps the most homogeneous cloud regime one could hope to find—nocturnal marine stratocumulus—and only at the level of the aircraft. Though not well suited to characterizing the vertical profile of divergence, these measurements raise the question if, by measuring the vertical profile of the horizontal wind using dropsondes launched from an aircraft, one could estimate the *vertical profile* of large-scale mass divergence. Presuming that it is possible in principle, the important practical question then becomes how many sondes would be required to get an estimate of the divergence that would be accurate enough given the typical scales of variation of the wind in the tropics.

Some back-of-the-envelope calculations provide context for this sampling problem. Consider the traditional view whereby in the boundary layer air motions are conceptualized as being composed of a small-scale and a large-scale component. In this case the large-scale divergence $D$ is defined as

$$D = \partial_x \overline{u} + \partial_y \overline{v}, \tag{1}$$

where $\overline{u}$ and $\overline{v}$ denote the large-scale zonal and meridional wind components, respectively. By this definition $D$ is proportional, through the density, to the *mass divergence*. Neglecting what amounts to a small effect from density variations with height, the large-scale vertical wind $\overline{w}$ can then be derived from continuity as

$$\overline{w}(z) = -\int_0^z D \, dz. \tag{2}$$

In the two-scale view, typical values of the integral length scale of horizontal velocity $l_x$ are taken to be about half the depth of the boundary layer, or about 300 m in the case that the boundary layer is identified with the subcloud layer. A typical velocity scale, $v_x$ of the small-scale turbulence is $1 \, \text{m s}^{-1}$ (Lenschow et al. 1999). If measurements are performed on scales much larger than $l_x$, then they can be considered independent so that the random contribution to the divergence measurement goes as $v_x/\sqrt{N}$. Hence for $D = 10 \times 10^{-6} \, \text{s}^{-1}$ over $L = 200 \, \text{km}$, the horizontal velocity difference over this distance is $D \times L = 2 \, \text{m s}^{-1}$ so that for a 20% error one would want $v_x/\sqrt{N}$ to be about $0.4 \, \text{m s}^{-1}$, which for $v_x = 1 \, \text{m s}^{-1}$ implies about six or seven sondes. However if $D$ is just 2 times smaller—as might be expected if the large-scale vertical velocity required to balance radiative cooling in the free troposphere is set up entirely by mass divergence within the boundary layer—then 25–30 sondes would be required. Another question is the extent to which, given the observed spectrum of horizontal velocity variance in the free troposphere (Nastrom et al. 1984; Li et al. 2018), this two-scale view is informative.

Mapes et al. (2003) use sounding data from ship arrays to estimate $v_x = 1.5$–$2.0 \, \mathrm{m \, s}^{-1}$ on a scale of few hundred kilometers. This would increase the sampling requirements by a factor of 2–4 to achieve the same accuracy, and it begins to raise practical concerns if $D$ becomes too small. These estimates suggest that the proposed method could be feasible but is by no means guaranteed. Its practicality depends crucially on the magnitude of $D$, whose magnitude and structure on the mesoscale within the free troposphere is not known.

These theoretical considerations provide guidance but are based on a conceptual model for the wind. In reality, relatively little is known about the actual structure and variability of the vertical wind on the meso-$\beta$ scale within the tropics. It thus also seems important to ask, How would one know if the proposed technique is actually suitable to measure $D$? One obvious answer is that independent measurements should agree. Here independent measurements can be performed by sampling the same air mass at different times, ideally separated in time by a period that is small compared to the period over which the large scale evolves (say, as measured by its decorrelation time scale) but large as compared to the time scale of the small-scale flow, which—from the perspective of $D$—acts as noise. Other approaches can also be used to assess the measurements, for instance, by comparing estimates of vertical motion inferred from the measurement of $D$ to other estimates, for instance, by tracking conserved tracers. Also checks of physical consistency, for instance, with the observed cloud field, may provide indirect assessments of the measurements.

This paper addresses these different questions and provides evidence, using all of the methods identified above, that it is actually possible to measure the vertical profile of mass divergence and vertical motion in the tropics by using dropsondes. Section 2 reviews the methodology through which $D$ and $\overline{w}$, but also the large-scale vorticity $\zeta$ can be inferred from wind measurements and presents the airborne field campaign. This section also presents the flight strategy that made it possible to test the technique. Section 3 presents the vertical profiles of divergence, vorticity, and large-scale vertical velocity estimated from the dropsondes. Sections 4 and 5 discuss the credibility, the error analysis, and the time and space representativity of the estimates, in part based on high-resolution simulations. An outlook of these measurements for the understanding of cloud–circulation couplings and for the modeling is presented in section 6.

## 2. Data and methodology

### a. Line integral and regression methods

As discussed by Holland and Rasmusson (1973), Nitta and Esbensen (1974), and Lenschow et al. (1999, 2007),

the definition of $D$ avails itself to an application of Gauss's theorem such that it should be possible to measure the mass divergence of the air over an area $A$ by using soundings or dropsondes distributed along the perimeter of this area. This method, referred to as the "line integral" method, infers $D$ at a particular level from horizontal wind measurements at that level and is expressed as follows:

$$D = \frac{1}{A} \oint V_n \, dl, \qquad (3)$$

where $V_n$ is the component of the horizontal wind normal to the perimeter of measurements. When applied to aircraft measurements, this method requires a stationary wind field.

An alternative method, referred to as the "regression method," has been proposed by Lenschow et al. (2007). It assumes that wind variations in longitude and latitude are linear at each vertical level, in effect defining the large-scale wind, such that

$$\mathbf{V} = \mathbf{V}_o + \frac{\partial \mathbf{V}}{\partial x} \Delta x + \frac{\partial \mathbf{V}}{\partial y} \Delta y, \qquad (4)$$

where $\mathbf{V}_o$ is the mean wind velocity over the area and $\Delta x$ and $\Delta y$ are the eastward and northward displacements from a chosen center point. The neglect of time derivatives (i.e., stationarity) is justified by virtue of the aircraft speed being much larger than the wind speed so that the sampling time scale is small compared to an advective time scale. Assuming stationarity also avoids issues that arise because the time and space sampling by the aircraft are not independent. As the comparison of estimates from the line integral and regression methods will show later, the stationarity assumption is actually not a bad assumption in our case. An approximate solution of this system can be found by computing the coefficients of a least squares fit to the wind field defined as Eq. (4), these just being the spatial and temporal derivatives of the large-scale wind field, which, by Eq. (1), is sufficient to determine $D$.

The large-scale vorticity $\zeta$ defined as

$$\zeta = \partial_x \overline{v} - \partial_y \overline{u}, \qquad (5)$$

can likewise be determined using the same methods: either the derivatives can be estimated directly from the regression method or (using Stokes theorem) as

$$\zeta = \frac{1}{A} \oint V_t \, dl, \qquad (6)$$

where $V_t$ is the component of the horizontal wind tangent to the perimeter of measurements.

## b. NARVAL2 campaign

This methodology was tested during the second Next-Generation Aircraft Remote Sensing for Validation Studies (NARVAL2; Stevens et al. 2016, 2017) airborne field campaign. NARVAL took place over the tropical Atlantic upwind of Barbados (13°N, 59°W) during the period from 8 to 28 August 2016 and consisted of 10 research flights of the German High Altitude and Long Range Research Aircraft (HALO) associated with a range of research objectives.

Two research flights (RFs), RF03 and RF06, which took place on 12 and 19 August 2016, were dedicated to testing the dropsonde method for estimating profiles of divergence and vertical velocity. Because the measurements were conceived for use in the Elucidating the Role of Cloud–Circulation Coupling in Climate( EUREC$^4$A) field campaign, which will take place in winter 2020 (Bony et al. 2017), flight operations were located away from regions of deep convection so as to provide a better analog to the conditions of the winter trades.

During these flights, HALO typically flew at an altitude 30 000 ft (about 9 km) above mean sea level where GPS dropsondes (Vaisala RD94; Wang et al. 2015) were intensively released. Each dropsonde measured the vertical profiles of pressure, temperature, and humidity with a vertical resolution of 5–10 m and a manufacturer-stated accuracy of 0.4 hPa, 0.2°C, and 2%, respectively. Equipped with a GPS receiver, the dropsonde also measured the instantaneous horizontal wind speed with an accuracy of 0.1 m s$^{-1}$. All dropsonde data were processed using the Atmospheric Sounding Processing Environment (ASPEN), version 3.3-270, software, and the data were further visually inspected for possible biases or malfunction before being interpolated onto a regular 10-m vertical resolution for the purposes of further analysis.

## c. Flight strategy

To test the ability of dropsondes to measure divergence and vorticity it was deemed optimal to fly circular flight patterns (Fig. 1). As discussed by Lenschow et al. (1999), such a pattern not only has the largest enclosed area of any closed curve of a given length, it further optimizes the use of aircraft time by eliminating the need to make sharp turns, during which data are not reliable. Pairs of alternating direction circle legs were flown to enable an eventual analysis of the flight-level winds from the gust probes (following Lenschow et al. 2007), although these are not analyzed here. More importantly, by repeating the measurements over pairs of circles, slightly offset to follow a rough estimation of the drift of the air mass over the time between the start of each circle, it becomes possible to independently assess the reproducibility of the measurements. If the measurement of $D$ and $\zeta$ around any one circle would be dominated by noise or sampling error or if the flow is not sufficiently stationary to make it possible to think meaningfully of a large-scale environment, then one would not expect successive measurements to be in accord with one another. Hence the reproducibility of the measurements across pairs of circles provides a critical test of the proposed method.

Several factors influenced the choice of circle size. For a flight level of 30 000 ft (FL300) sondes would begin measuring at an altitude of about 9 km and take about 740 s to descend to the surface. Because the dropsonde system being used on HALO could only track four sondes at once, this implied that the preparations for the launch of the fifth sonde could only begin 740 s after the launch of the first sonde. Allowing 90 s for the preparation and launch of a sonde, so as to have a small buffer in case of a malfunctioning sonde, implied a spacing of at least 3.5 min between launches, or a minimum circle size of 42 min. It turns out that even if sondes could be launched more frequently, a circle of at least this size would be desirable so as to survey a sufficiently large area and to minimize the roll angle of the aircraft, which influences the performance of other instruments used for purposes of remote sensing. For a 45-min circle at FL300, HALO circumscribes a circle of about 170 km in diameter, with a roll angle of about 2°–3°. Attempts have been made to discern the effect of this small roll on other measurements made on HALO, but none has been identified.

Figure 2 shows the visible imagery from MODIS for 12 and 19 August (left and right panels, respectively), with the general area of flight operations indicated by circles shifted following the mean flow to the time of the satellite overpass. As the images show, as is further discussed in section 4, the measurements were made in relatively undisturbed, or even suppressed, conditions. The MODIS (on *Aqua*) overpass occurred between the time of the circle pairs. Individual circles were also flown on other flights, and near and around regions of more disturbed flow, with the idea that they could be analyzed in the event that the test of the method during RF03 and RF06 proved it to be satisfactory. Figure 1 describes the actual positions of good (quality controlled) soundings. Two pairs of circles were flown in different areas on each flight, so that each of the four panels in Fig. 1 corresponds to a pair of circle legs, and what we assert to be an independent measurement. Sonde positions are given by the last recorded (near surface) latitude and longitude. For the most part sondes are well distributed around a circle. The goodness of fit relative to a perfect circle is measured by the degree to which the sonde locations lie on the dotted line describing the least squares circle fit to
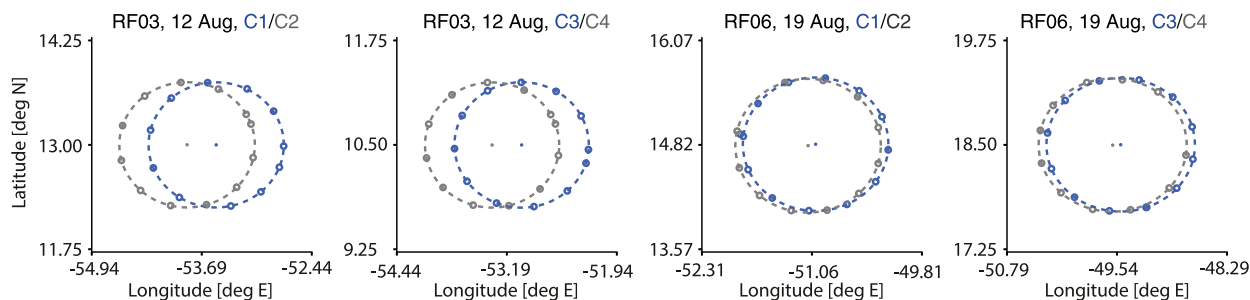
FIG. 1. Pairs of dropsonde circle flight legs flown on RF03 and RF06 on 12 and 19 Aug 2016, respectively. The circular legs are enumerated separately for each flight. The markers indicate the position of the sondes dropped from the aircraft.

the last measured position of each sonde. On these test flights all of the sondes were launched from FL300, began measuring winds at an altitude of about 9 km, and reached the surface about 740 s later. For a mean, relatively barotropic, wind of $7\,\mathrm{m\,s^{-1}}$ this corresponds to a lateral displacement of about 5 km over the descent, which is actually what was observed and about the diameter of the marker used to indicate the sonde position in Fig. 1. Additional information about the circle legs is provided in Table 1.

Slight differences in the execution of the flight plan can be discerned from Fig. 1. On RF03 the pilots were asked to circumscribe a circle in 45 min so that the twelfth sonde would nearly overlap with the first. To allow for a more regular distribution of the sondes, and a less hectic release schedule, the flight time allocated for each circle leg was slightly increased, to 48 min, on

RF06. As a result the best-fit circle radius increased from 83.5 km for the circle legs on RF03 to 89 km for the legs on RF06. A weaker mean wind ($6\,\mathrm{m\,s^{-1}}$ on RF06 vs $8\,\mathrm{m\,s^{-1}}$ on RF03) also meant that during RF06 the second circle within each pair was less displaced from the first as compared to RF03.

The relative humidity and static stability profiles measured by the dropsondes help characterize the meteorological situation sampled by the sondes. As shown by Fig. 3 a well-mixed boundary layer of depth 500–600 m is well demarcated by the low values of static stability and increasing relative humidity. The top of this layer is identified by the local maximum of relative humidity. Above this a cloud layer, whose depth varies considerably across the soundings, is indicated by a moist layer extending up to the level where the stability increases sharply (around 1.5–1.8 km). This local
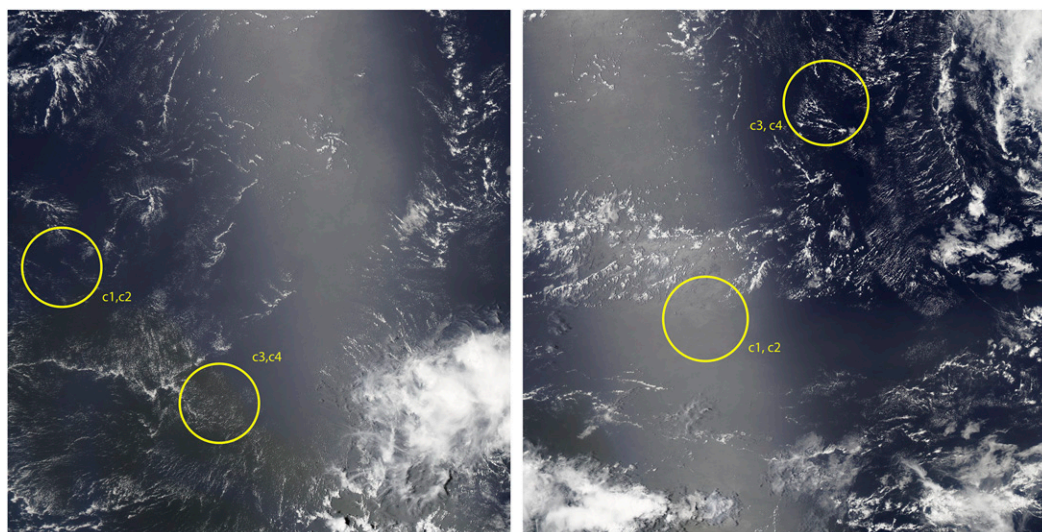


FIG. 2. MODIS Worldview 10° × 10° visible images: (left) RF03 on 12 Aug 2016, centered at 13°N, 52°W, and (right) RF06 on 19 Aug 2016, centered at 15.5°N, 50°W. The approximate location of the circle pairs is shown, adjusted by the mean wind to the time of the satellite overpass. For these calculations a 1640 and 1648 UTC overpass time was adopted for RF03 and RF06, respectively.

TABLE 1. Start and end times, center point, diameter, and mean (sonde integrated) magnitude of the 10-m horizontal wind and sea surface temperature of each of the main sounding circles legs during RF03 (12 Aug 2016) and RF06 (19 Aug 2016).

| Flight | Leg | Start–end times (UTC) | Lat (°N) | Lon (°E) | Diameter (km) | Wind (m s$^{-1}$) | SST (°C) |
|---|---|---|---|---|---|---|---|
| RF03 | C1 | 1306–1348 | 13.01 | −53.49 | 168 | 6.1 | 28.1 |
| | C2 | 1357–1441 | 13.00 | −53.83 | 168 | 6.0 | 28.1 |
| | C3 | 1655–1739 | 10.49 | −53.01 | 168 | 7.6 | 29.0 |
| | C4 | 1746–1830 | 10.50 | −53.34 | 168 | 7.9 | 29.1 |
| RF06 | C1 | 1346–1434 | 14.84 | −51.08 | 180 | 5.3 | 27.8 |
| | C2 | 1440–1524 | 14.74 | −51.06 | 180 | 4.6 | 27.8 |
| | C3 | 1710–1758 | 18.42 | −49.47 | 180 | 6.4 | 27.5 |
| | C4 | 1804–1848 | 18.36 | −49.64 | 180 | 6.6 | 27.6 |

maximum in the static stability exceeds 0.1 K hPa$^{-1}$, and is associated with a sharp hydrolapse (with relative humidity decreasing from 80%–90% to 20% in less than 1 km), and we identify this feature with the trade inversion. The layer between the trade inversion and the top of the boundary layer can be associated with the layer of shallow convection and is least pronounced in the sondes from the first pair of circles during RF03. In RF03 an elevated moist layer with relative humidity ranging from 40% to 60% extends from 3 to 4 km, topped by a second inversion layer near the 0°C isotherm

that is located at about 4.5 km. This elevated moist layer is less evident in RF06 and more generally absent during winter (Stevens et al. 2017). It likely results from the midtropospheric outflow of moist air from remote convection or from the remnants of past midlevel convective events. Above the 0°C isotherm, the troposphere is extremely dry, as expected in regimes of suppressed convection. All the measurements show an indication of enhanced stability and progressively drier air between 4.5 and 7.5 km. The enhanced stability at midlevels and the presence of the trade inversion (even deep within the
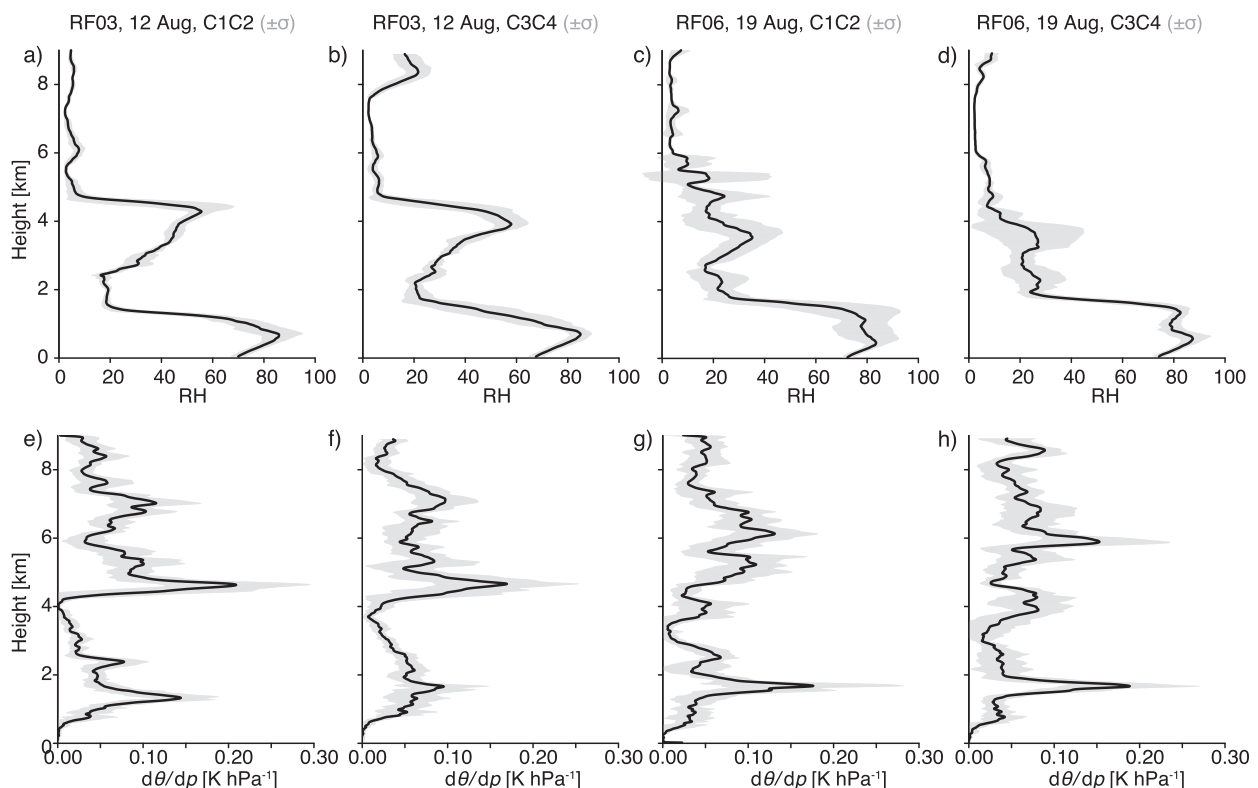


FIG. 3. Vertical profiles of (a)–(d) relative humidity and (e)–(h) static stability derived from all the dropsondes launched along a pair of circular flights (24 sondes). The shading represents plus and minus one standard deviation among the 24 soundings. Profiles are from (a),(b),(e),(f) RF03 (12 Aug) and (c),(d),(g),(h) RF06 (19 Aug).
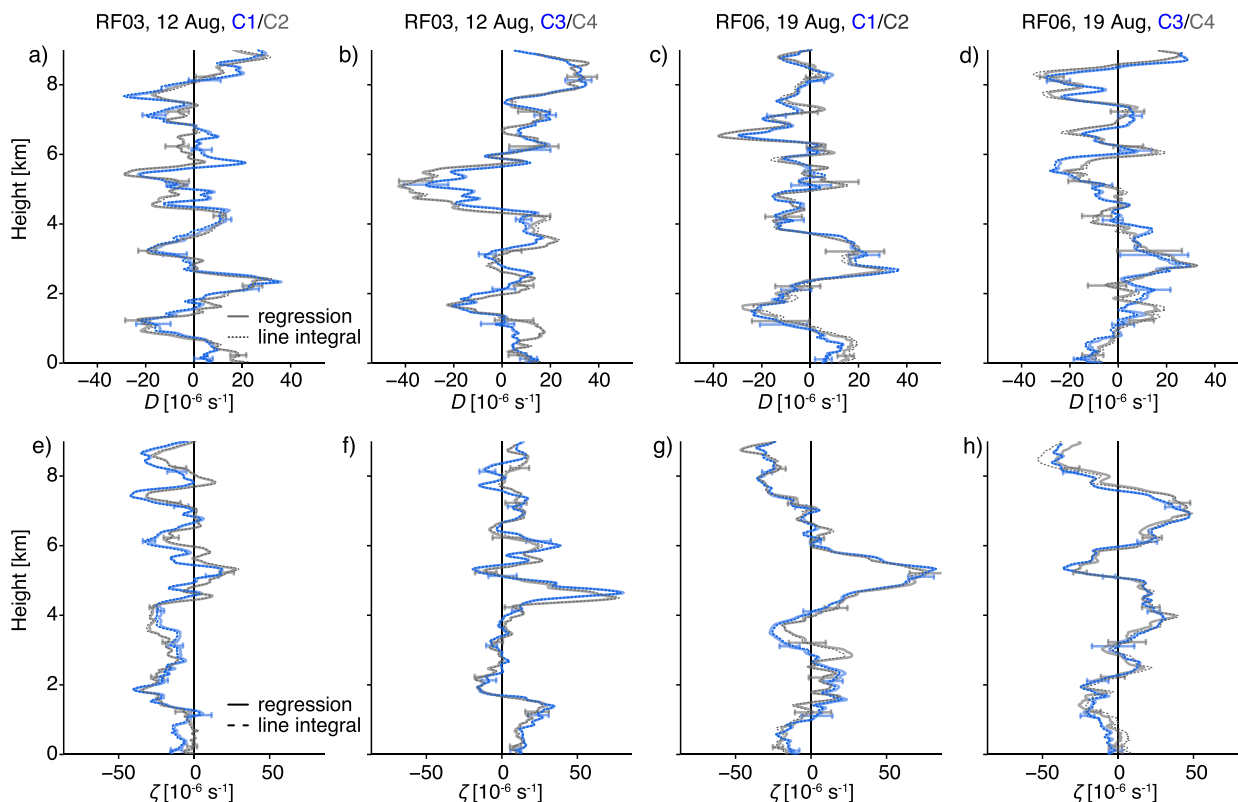
FIG. 4. Vertical profiles of (a)–(d) large-scale mass divergence and (e)–(h) vorticity estimated from the dropsondes wind measurements performed during (a),(b),(e),(f) RF03 (12 Aug) and (c),(d),(g),(h) RF06 (19 Aug) along each circular flights (the first circle is in blue, and the second one is in gray), using either the regression method (solid line) or the line integral method (dashed line). Horizontal bars represent plus and minus one standard error of the regression estimate, and for the sake of clarity, they are shown at selected vertical levels only.

tropics) also emerge as robust features in the soundings taken over the western Pacific during TOGA COARE, as documented by Johnson et al. (1996).

## 3. Estimates of divergence and vorticity

### a. Measured profiles of $D$ and $\zeta$

The analysis suggests that just 12 dropsondes released around a circle provide a viable way to measure $D$ and $\zeta$ over the area circumscribed by that circle. This conclusion is substantiated by Fig. 4, which presents the vertical profiles of $D$ and $\zeta$ calculated using both the line-integral and regression methods applied to the dropsonde measurements from the RF03 and RF06 circle pairs. The two estimates of $D$ profiles across a pair of circles within the same air mass are hardly distinguishable; if anything the measurements of $\zeta$ differ across pairs of circles even less than do estimates of $D$ Alternating extrema in estimates of $D$ on a vertical scale from 1 to 2 km agree in both magnitude and location across a pair of circles. Even smaller-scale features, for example, the variability in

$D$ between 4 and 6 km in the first pair of circles from RF06, are well reproduced from one circle to the next.

An advantage of the regression method is that estimates of the uncertainty in the regression can be obtained. These uncertainty estimates are included as error bars overlying on the profiles in Fig. 4. They further substantiate the viability of the proposed methods for estimating profiles of $D$ and $\zeta$; as the uncertainty of the regression is commensurate with the differences between estimates across a circle pair. That these measurements are indicative of the large-scale wind, and not unduly influenced by sampling errors from smaller-scale velocity fluctuations, is also attested to by the similarity between the line-integral and regression-based estimates of $D$ (and $\zeta$), as the former make no assumption about the structure of the large-scale wind but does require stationarity, which would not be expected for small-scale perturbations.

To the extent that Fig. 4 attests to a surprisingly high degree of accuracy and precision in the dropsonde-based estimates of $D$ and $\zeta$, it also highlights some other surprising features. Hence, even though the purpose of the

present study is to demonstrate the viability of the dropsonde method for estimating $D$ and $\zeta$, because they provide insight into aspects of the tropical atmosphere that have never before been observed, these features merit a brief comment. They include the following:

- Large horizontal variability in $D$ as measured across pairs of circles: on 19 August (RF06), for instance, the subcloud layer (which extends over the first 500–600 m of the atmosphere) is associated with a mass divergence in the southern circles (C1 and C2) but with a mass convergence in the northern circles (C3 and C4). On 12 August, the middle troposphere exhibits a peak of mass convergence and a peak of positive vorticity in the southern circles (C3 and C4) close to the ITCZ, which are not found in the northern circles (C1 and C2).
- A surprisingly large amplitude and vertical variability in $D$ and $\zeta$ on vertical scales from 1 to 2 km. The radiatively driven subsidence (defined as $w = \dot{Q}/(\Gamma - \Gamma_d)$, where $\Gamma$ and $\Gamma_d$ are the actual and dry adiabatic lapse rates, respectively, and $\dot{Q}$ is the clear-sky atmospheric radiative cooling), which climatologically must characterize the large-scale atmosphere, can be sustained by a value of $D = 5 \times 10^{-6} \, \text{s}^{-1}$ confined to a layer of about 1 km in depth. In the measurements, values of $D$ within the subcloud layer can be twice this value. More surprising is the magnitude of the variability in $D$ within the free troposphere, which is about $20 \times 10^{-6} \, \text{s}^{-1}$. This suggests that within the free troposphere the divergence of mass in layers of 1 km can be 4 times larger than the climatological divergence driven by radiative cooling.
- Some commonalities across the four sets of circles are also apparent. The divergence within the boundary layer varies weakly with height and usually is associated with convergence within the trade-inversion layer (which extends from about 1.5 to 2.5 km); in the lower troposphere, all profiles exhibit a layer of positive vorticity in the midtroposphere near the freezing level and an extremum of low-level vorticity in association with the greatly enhanced stability near the base of the trade inversion. Finally, spectral and autocorrelation analyses of the divergence profiles show a clear dominance of a wavelength of 2–3 km in the vertical (not shown).

Some of the common features share similarities to earlier airborne Doppler radar–based estimates of divergence made during less suppressed conditions during the TOGA COARE campaign (Mapes and Houze 1995). Those measurements also indicated the presence of wavelike oscillations of the divergence field (but with a vertical wavelength of about 4 km) pinned to a persistent layer of midlevel convergence near 4.5–5.0 km. Mapes and Houze

interpreted these features as the result of the adjustment of the atmosphere to the mesoscale cooling associated with the melting level (see also Johnson et al. 1996), something they referred to as "melting reverberations." Numerical studies of the response of the stratified atmosphere to heating (Holton et al. 2002; Alexander and Holton 2004) suggests that many of these features could be compatible with large-scale inertial gravity waves, which by the evacuation of mass out of the layer could be expected to increase its relative vorticity. Three of the four sets of soundings show a vorticity maximum near the 0°C isotherm (near 4.5–5.0 km), two of which are associated with a layer of mass divergence. We can speculate that the reverberations referred to by Mapes and Houze are forced not just by phase changes but also from radiative processes. The latter would also act on the sharp humidity gradients at the top of the subcloud layer and at the top of the trade inversion (Stevens et al. 2017). This, condensational heating in cloud layers from 1 to 2 km, and cold pools from shallow precipitation spreading through the subcloud layer, all provide heating on vertical scales ranging from 0.5 to 2 km. Hence we hypothesize that the more general vertical structure of the divergence field reflects reverberations of remote radiative and condensational heating, also from layers of more shallow convection—an idea we look forward to testing in subsequent work.

### b. Sensitivity to the number of sondes

Returning to a central question of this study, here we ask whether we can use the measurements to assess how many sondes are necessary to characterize the large-scale mass divergence on the scale of an individual (170-km diameter) circle. For a given day and a given air mass (C1 and C2 or C3 and C4), the two $D$ estimates computed by using 12 sondes along each circle are in good agreement. To get an ever more statistically robust estimate of the large-scale divergence within each air mass, we compute $D$ using the regression method and all the dropsondes (24) launched within the air mass along both circles. This "best estimate" of the vertical profiles of $D$, and the 5%–95% confidence interval that comes with it, can be used to estimate the impact of systematically reducing sondes from the analyses.

This allows us to ask, using the measurements alone, What error arises relative to the best estimate of $D$ if we reduce the number of sondes within a circle or distribute the same number of sondes across two circles, thereby having fewer sondes along each circle? For this purpose, we sample every second, or every third sonde along each circle, and consider either a single circle or two circles (with the same number of sondes). Then we compare the discrepancy between the best estimate of $D$ (obtained with the maximum number of sondes: i.e., 24 sondes
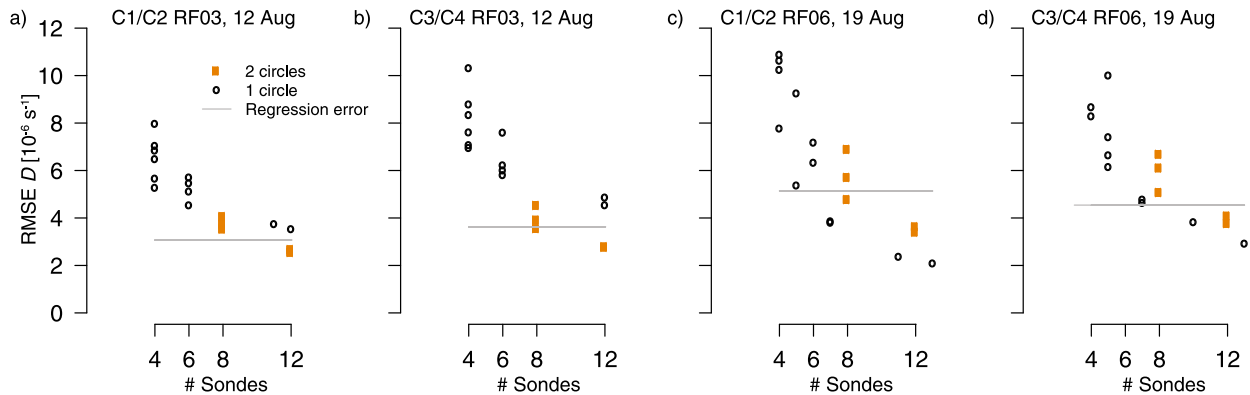
FIG. 5. RMS difference between the lower-tropospheric divergence ($D$ averaged over the first 5 km) estimated using 24 sondes (two circles of 12 sondes each) and that estimated using fewer sondes, distributed along one circle (open markers) or two circles (filled circles). Also reported (gray line) is the mean statistical error associated with the regression estimate of $D$ for 24 sondes.

distributed over two circles) and the estimate $\tilde{D}(z)$ obtained with a reduced number of sondes (evenly distributed along each circle) and/or a reduced number of circles. This discrepancy is quantified by the root-mean-square error (RMSE) between $D(z)$ and $\tilde{D}(z)$ averaged over the lower 5 km of the atmosphere (comprising nearly 500 data levels). The RMSE is then compared to the 5%–95% confidence interval of the $D(z)$ estimate derived from the regression method, also averaged over the lower 5 km.

As expected, the RMSE increases as the total number of sondes decreases (Fig. 5). Using two circles with six sondes along each circle provides $\tilde{D}$ estimates that remain within the statistical uncertainty of $D$. Using only one circle with 12 sondes can be sufficient to estimate $D$ in some cases (e.g., RF06) but not so well in other cases (e.g., RF03). On the other hand, using less than eight sondes in total is generally not adequate. These four examples thus suggest that no less than 12 sondes should be used to estimate $D$ on a scale of $O(100)$ km. In this example distributing the sondes along two successive circles improves the estimate, but it is unclear if this has to do with the fact that the best estimate also samples this longer time interval.

## c. Large-scale vertical velocity

The apparent accuracy of the best estimate of the divergence profiles encourages inspection of the vertical profile of large-scale pressure velocity $\omega$ of an air mass that it implies. Using Eq. (2), the pressure velocity can be expressed in terms of $w$ such that

$$\omega(z) = -\rho(z)gw(z), \qquad (7)$$

where $\rho$ is the density and $g$ the gravitational acceleration. Figures 6a–d show the vertical profile of the best

estimate of $D(p)$, that is, the divergence calculated from the regression method using all the dropsondes (24) launched within a given air mass, together with the 5%–95% confidence interval associated with the regression estimate. In Figs. 6e–h the corresponding estimate of $\omega$ is given as a function of height.

The four pairs of circles show common features: the large-scale vertical velocity $\omega$ exhibits two extrema (positive or negative), one in the lower troposphere near the top of the subcloud layer and another one in the mid-troposphere near the 0°C isotherm, and it nearly vanishes around 2 km and around 6–7 km. In the free troposphere, the large-scale subsidence maximizes around 4 km with rates of about 5 hPa h$^{-1}$, while at the base of the trade inversion, $\omega$ maximizes with a rate of about 3–4 hPa h$^{-1}$ in the subsidence cases and about $-3$ hPa h$^{-1}$ in the convergence case. In the lower troposphere, these values are roughly consistent with the magnitude of estimates inferred, in roughly similar meteorological conditions, from measurements made during BOMEX (Nitta and Esbensen 1974) and ASTEX (Ciesielski et al. 1999).

## 4. Credibility and error analysis

The previous section showed that it is possible to accurately and precisely measure vertical profiles of large-scale vertical motions from dropsondes and that the profiles thus derived appear to primarily characterize the large-scale environment rather than be dominated by unrepresentative small-scale flow features. In this section, we go one step further in the assessment of the credibility of the vertical motion estimates. First, we assess their consistency with the observed cloud field and then with atmospheric simulations of the NARVAL2 campaign run using a dynamical model capable of resolving mesoscale motions on the scale of a few kilometers and initialized by
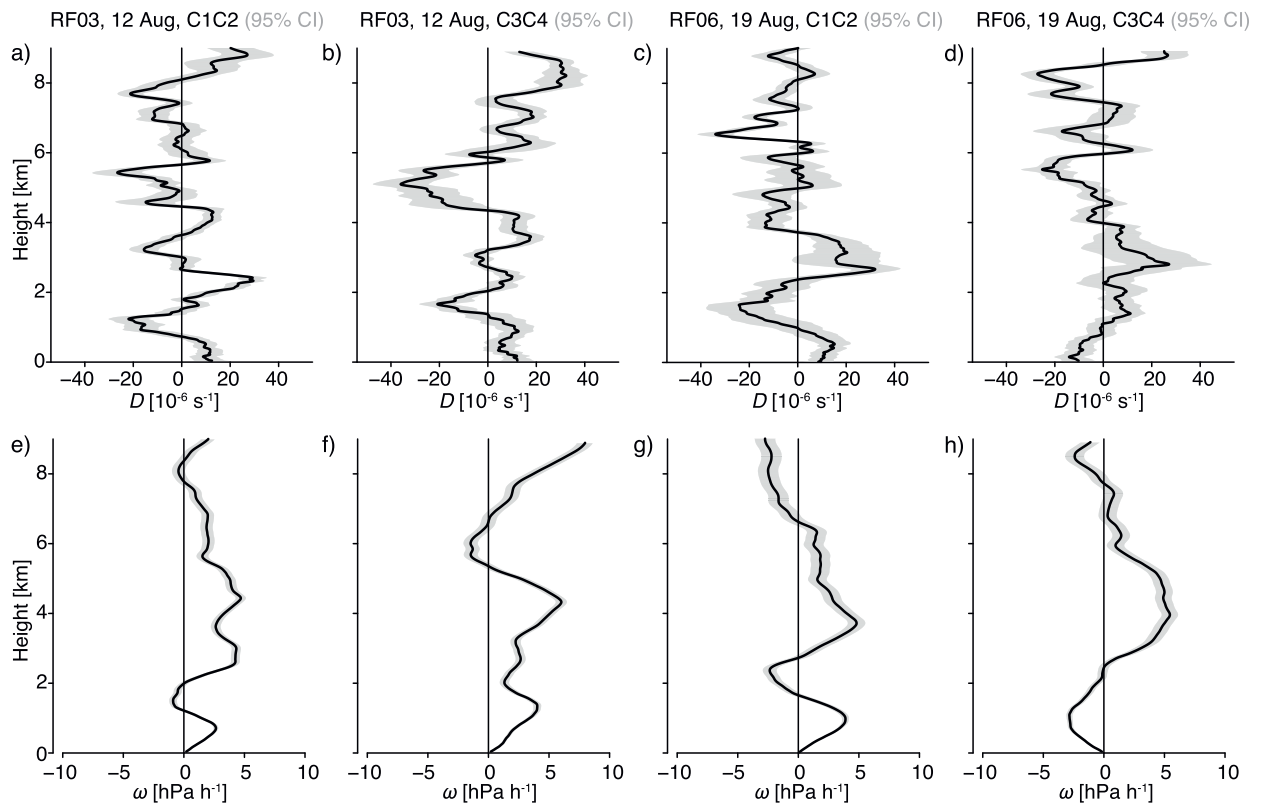
FIG. 6. Vertical profiles of (a)–(d) large-scale mass divergence and (e)–(h) vertical velocity estimated (using the regression method) from all the dropsondes launched along a pair of circular flights (24 sondes). For each pair of circles, the shading represents the ±5%–95% confidence interval of regression estimates. Profiles are from (a),(b),(e),(f) RF03 (12 Aug) and (c),(d),(g),(h) RF06 (19 Aug).

meteorological analyses to reflect the observed flight conditions.

### a. Observed cloud field

Visual inspection of the cloud fields observed from the aircraft and by satellite provides a reality check of the measurements of $D$ and $\omega$ (Fig. 2). In regions of low-level divergence one expects the clouds to be more suppressed relative to regions of large-scale low-level convergence. Focusing first on RF03, both pairs of circles show substantial divergence, and hence subsidence, over the lower kilometers of the atmosphere. The main difference is that in the second pair of circles, flown more to the south, the divergence is over a deeper area. Consistent with these measurements, both circles show only a dusting of very shallow cumuli (with lidar-derived cloud tops around or below 2.0 km; Stevens et al. 2017) and little spatial organization on the scale of the measurements.

In RF06 the situation is different as a somewhat cloudier area was deliberately targeted for the second pair of circles. In the first pair of circles, C1 and C2, the northern leg of the circle pair crossed a strong dust

gradient, with less dust-laden air and a thin layer of stratiform clouds on the very northern fringe of the circle, but over the bulk of the circle (between what would be 2 and 10 o'clock if the circle would describe a clock with 12 o'clock being due north) the atmosphere was dust laden, and conditions appeared quite suppressed. The few clouds that were evident barely rose out of the boundary layer, with a vertical extension rarely exceeding 1.5 km. The second pair of circles told a very different story. There, active convection with precipitating clouds rising above 2 km were evident from the flight deck throughout most of the circle. The contrast is better illustrated in Fig. 7, which zooms in on the flight areas outlined in Fig. 2. A thin veil of grayer clouds near the 5 o'clock position on the circle is indicative of deeper precipitating convection. A much more active layer of shallow convection was also evident from the flight deck. A radar signature along C3 and C4 was also evident as compared to along C1 and C2, where cloudiness did not sufficiently develop to be detected by the cloud radar. This is consistent with measurements of $D$ (Fig. 6), which show modest convergence in the lower 1 km of the atmosphere along C3 and C4, as compared to strong divergence in the area measured by
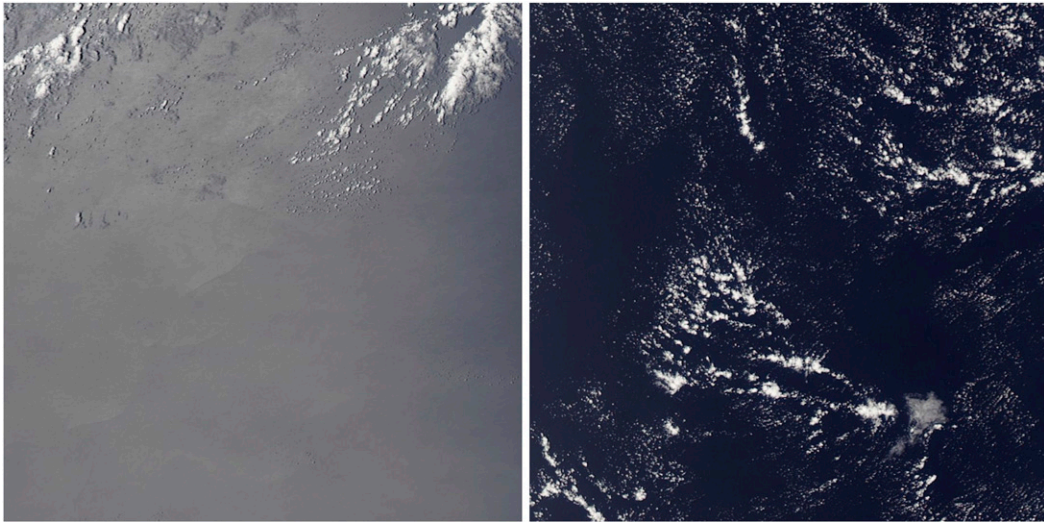
FIG. 7. MODIS Worldview $2° \times 2°$ visible images centered on the mean wind-shifted positions of circles (left) C1 and C2 and (right) C3 and C4 of RF06. The brighter background in C1–C2 is mostly a result of sun glint but also is influenced by greater dust loading.

C1 and C2. Whereas the low-level vertical motion is downward and maximizes with a value near $5\,hPa\,h^{-1}$ over C1 and C2, over C3 and C4 it is directed upward with a magnitude near $-3\,hPa\,h^{-1}$. These measurements are thus qualitatively quite consistent with expectations based on the observed cloud field—and thereby provide the desired reality check.

### b. Lagrangian estimates of large-scale vertical velocity

The vertical moisture structure during RF03 also provides an opportunity to estimate the large-scale vertical motion by tracking water vapor and thus more quantitatively assess the dropsonde-based estimates of $\omega$. Particularly along C1 and C2 there was a well-defined gradient in water vapor near the 0°C isotherm, which sloped downward through the atmosphere across the circle. This feature, thought to be associated with outflow of moisture from convection to the southeast, was more extensively analyzed by Stevens et al. (2017). Profiles of moisture and temperature from the sondes launched around C1 and C2 are shown in Fig. 8.

If we assume that the moist layer that extends to the inversion around the 0°C isotherm is a Lagrangian feature, we can track its descent by the slope of the surface along the direction of the mean wind. To do so we calculate the slope of this surface by regressing the pressure height of the $2\,g\,kg^{-1}$ specific humidity isosurface, which we call $p_2$, from each of the sondes against the position of the sonde:

$$\omega = \partial_t p_2 - \mathbf{V} \cdot \nabla_h p_2. \qquad (8)$$

Then assuming that this spatial feature arises solely from advection, it follows that the downward velocity is just the dot product of the winds along $p_2$. From Fig. 8, $p_2$ across the circle is about 30 hPa. This difference is primarily in the zonal direction, with the zonal wind being about $-8\,m\,s^{-1}$ at this level. For a 180-km circle this translates into about a parcel transit time across the circle of 0.25 days. Hence the implied subsidence would be about $130\,hPa\,day^{-1}$. Carrying out the calculation more precisely using the regressed slope and winds yields an estimate of $116\,hPa\,day^{-1}$. The vertical velocity derived from the sonde-based estimates of divergence yields a value of $102 \pm 5\,hPa\,day^{-1}$ averaged between 575 and
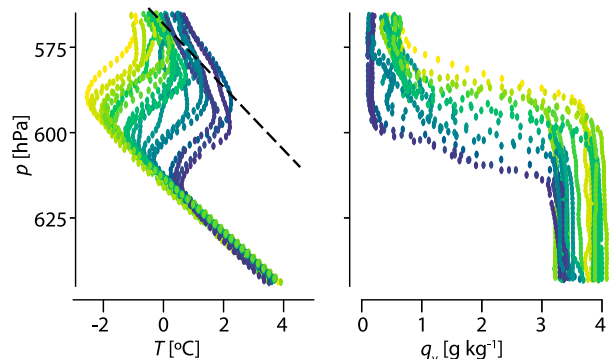


FIG. 8. (left) Temperature and (right) specific humidity in a roughly 1-km-deep layer (between 650 and 560 hPa) about the melting level for the sondes launched during C1 and C2 of RF03. Individual soundings are colored by the height of the $2\,g\,kg^{-1}$ specific humidity isosurface, which systematically descends from the east (where it is highest) to the west, across the circle. The dashed line shows the slope of a dry adiabatic temperature profile.

600 hPa. This level of agreement is reassuring, particularly because the measured subsidence velocity is considerably larger than would be expected by assuming that away from deeper convection the subsidence warming balances the radiative cooling of the atmosphere.

The inference that the atmosphere is subsiding at a rate much larger than that required to balance its radiative cooling is consistent with the observed temperature profile. In the limit where the atmosphere is subsiding much more rapidly than can be balanced by its radiative cooling, we expect the temperature profile to follow the dry adiabat. Above the cold point, which can be associated with the strong radiative cooling from the top of the elevated moist layer, we expect the radiative contribution to the temperature change as an air parcel descends to be much smaller than its adiabatic warming. In Fig. 8 it is apparent that the descent of the top of the temperature inversion near the 0°C isotherm very much follows the dry adiabatic profile, consistent with the observation of subsidence velocities much greater than what would be expected if they were merely balanced the radiative cooling of the layer.

### c. Inferences from modeling

In assessing the credibility of the measurements three questions arise that can be addressed by simulating the observed case using models run at much higher resolution than the scale of the desired divergence estimates. For this purpose we use the storm-resolving Icosahedral Nonhydrostatic (ICON) simulations described by Klocke et al. (2017). We use the simulations to determine whether (i) the unexpectedly large magnitude and rich vertical structure of the divergence is also apparent in the simulations, (ii) the apparently small error is consistent with what one would find by sampling the simulations in a consistent way, and (iii) the values of $D$ and $\omega$ are representative of what one finds in the model. This last question also addresses one of the initial assumptions of our analysis: namely, spatiotemporal scale of variability in the divergence field that we endeavored to measure.

We analyze simulations for both the December 2013 and August 2016 periods encompassing the NARVAL and NARVAL2 field studies. The simulations were initialized from, and nudged at their boundary, using data from the Integrated Forecast System (IFS) of the European Centre for Medium-Range Weather Forecasts. A simulation was started on each day of the respective month and run for 36 h, leading to a 12-h overlap between pairs of simulation and allowing us to discard the initial 12 h of each simulation to minimize issues in spinning up convective and turbulent fields. The domains consisted of two meshes, an outer (2.5 km) mesh spanning a large part of the tropical Atlantic (5°S–20°N, 64°W–10°E) and

an inner (1.25 km) mesh covering the area of flight operations (4°S–18°N, 64°–42°W). Analysis is performed only over the finer inner mesh using three-dimensional fields output hourly on their native computational mesh.

We mimic the aircraft operations by defining a flight path consisting of the set of points equidistant from a prescribed point—a flight circle. Along the circle, vertical profiles of desired fields are extracted at specific points, corresponding to virtual sonde drops. This drop point is selected by evenly distributing a number of virtual drops around the circle, as was done in reality. Measurement error was introduced by adding a random component to the drop position by adding a random Gaussian positioning error of 5% to both the angular offset between pairs of sondes (standard deviation) and to the radius (as defined in terms of polar coordinates about an origin located at the circle center point) of the intended drop position. Each component of the horizontal wind vector $\mathbf{V}$ was given a random Gaussian error with a standard deviation of $0.5\,\mathrm{m\,s^{-1}}$, which is a conservative estimate. The true value of divergence was taken to be the value derived in the absence of positional and wind errors and as obtained from 120 virtual sondes.

Some simplifications were introduced to ease the analysis. Virtual sondes were assumed to remain in a single atmospheric column, taken to be that column nearest to the virtual drop point. In reality during NARVAL2 the mean drift of the sondes was several kilometers. This simplification is justified by recognizing that this drift is commensurate with the model resolution and is small compared to the size of the circles being considered. The temporal evolution of the drops is also not considered in our analysis. Specifically we assume that all the sondes around a virtual circle are dropped at a single point in time. Because the results were insensitive to whether we took the hour of output that was closer to the time at which a real flight circle was initiated, or closer to the time when the circle terminated, and because, as shown below, the autocorrelation time of the fields was markedly longer than an hour, this simplification is also not a limiting one.

Based on this analysis we conclude that the vertical velocity and divergence field simulated by ICON are quite consistent with what was observed. This is shown in Fig. 9, which presents $D$ and $\omega$ from the dropsonde analysis and as calculated from ICON output. Because ICON is not a perfect model, and even for a perfect model the chaotic evolution of the fluid would cause small differences in the initial conditions to lead the model evolution to diverge from the observed state, we do not expect the ICON simulations and the sondes to agree perfectly. What we hoped to see was that the vertical structure in $D(z)$ as evident in the observation is
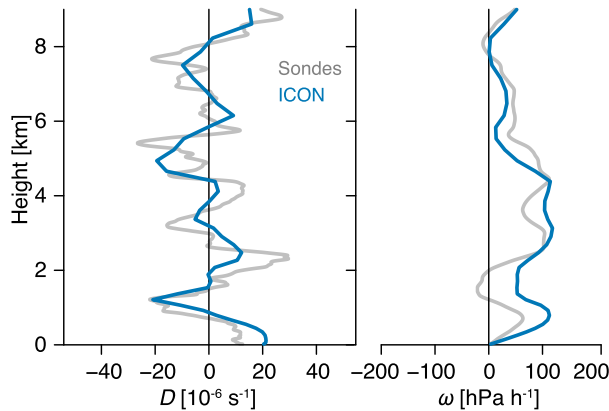
FIG. 9. Comparison of the vertical profiles of (left) large-scale divergence and (right) vertical velocity derived from dropsondes and from 120 perfect sondes around a circle in the ICON simulations at the location of the first pair of circles (C1 and C2) flown on 12 Aug 2016.

reproduced in the simulations. This is indeed the case, as both ICON and the sondes show a dominant vertical mode in $D$ to have a vertical wavelength between 1.5 and 2.5 km with a magnitude that is about $20 \times 10^{-6} \, \text{s}^{-1}$. The main features of the $\omega$ field are likewise reproduced, including the maximum near the top of the subcloud layer and the elevated maximum between 1.5 and 2.5 km. The degree of agreement is rather good for this case, surprisingly so actually. The simulations suggest that to the extent the simulated atmosphere is representative of nature, we could have expected the dropsonde method to work. Alternatively one could conclude that the simulated wind fields are, from the perspective of $D$ and its variability with height, similar to what was observed.

## 5. Spatiotemporal variability in $D$ and its implication for observations

The above analysis gives us confidence in the use of ICON to quantify sources of errors in measuring large-scale divergence from aircraft dropsondes. To quantify the magnitude of measurement errors we compare the RSME of divergence estimates from a small number of virtual sondes with random positional and wind errors as compared to estimates from perfect drops using 120 sondes. This exercise is analogous to that performed with the actual measurements as discussed in section 3b, but here we compare the RMSE over the lower 5 km to the standard deviation of the daily divergence estimates so as to compare the error in the estimated signal derived from a given number of sondes to the day-to-day variability in the simulated field. The simulations allow us to repeat this analysis for different sizes of circles and different numbers of sondes.

Overall the errors that we estimate from the analysis of the simulations are consistent with estimates of uncertainty derived directly from the divergence analysis. Figure 10 shows the comparison of the RMSE averaged over the lower 5 km of the atmosphere (comprising 30 model levels and denoted by open circles) in comparison to the daily standard deviation of the divergence $\sigma_D$ for the entire August period. There are several things to take away from this figure: (i) the magnitude of daily $\sigma_D$ for a circle of radius 100 km is about $1 \times 10^{-5} \, \text{s}^{-1}$, or about half the peak value of $D$ shown in Fig. 9; (ii) the day-to-day variability of the divergence decreases as the circle increases in size, approximately as the inverse of the size of the circle $r$—the blue line denotes the $\sigma_D \propto r^{-0.91}$ relationship; (iii) for reasons that are not clear to us, the error from estimating the divergence using a subsample of sondes, each with imposed random errors in the positioning of the virtual sonde location and in the winds they measured, appears to be a constant fraction of $\sigma_D$, irrespective of the size of the circle, and this error is also always smaller than the signal, even for as few as six sondes; (iv) the RMSE decreases with increasing number $N$ of sondes, roughly as $1/\sqrt{N}$, as one would expect. Thus, the RMSE decreases by about a factor of 2 (from 0.64 to 0.29) when increasing $N$ fourfold (from 6 to 24).

We have repeated this analysis for estimates of $\zeta$ and $\omega$, without random velocity and position errors, and for the December conditions. For circles of radii equal or larger than 100 km, random errors in $\zeta$ are about half as large as for $\omega$ and $D$, which are similar, and this error is dominated by sampling rather than random measurement error. For smaller ($\leq$50 km) circles, the error characteristics of $D$ and $\zeta$ become more similar, and estimates of $\omega$ become relatively larger. For the December simulations the results are similar, albeit with a slightly flatter ($\sigma_D \propto r^{-0.81}$) slope. Overall with 24 sondes the RMSE is $0.3\sigma_D$ for random wind errors of $0.5 \, \text{m s}^{-1}$. This reduces to $0.2\sigma_D$ if smaller ($0.2 \, \text{m s}^{-1}$) random wind measurement errors are assumed. If, consistent with Fig. 9, we take the amplitude of the typical divergence to be $2\sigma_D$, this implies an error of about 10%–15% in estimates of $D$ using 24 sondes.

The fact that $D$ decreases with increasing length scale or circle radius (Fig. 10) is, on the one hand, not surprising—eventually on the global scale the divergence must vanish. On the other hand, we are far from the global scale, and the fact that $\sigma_D$ varies inversely with the radius $r$ of the circle over which it is measured bespeaks the typical idealization used in almost every study of boundary layer clouds. There it is assumed that divergence is constant, and mean vertical motion is set by radiative processes on scales much larger than the
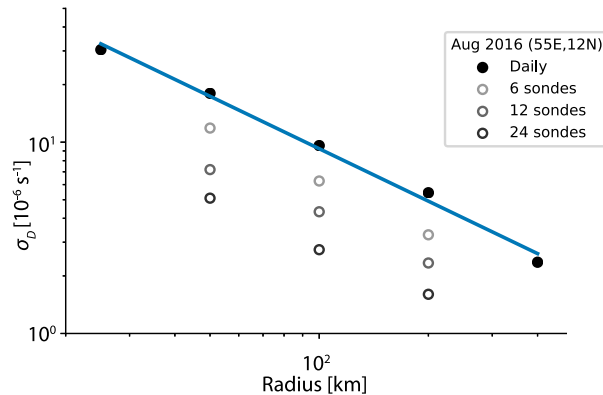
FIG. 10. Comparison of day-to-day variability in $D$ (closed circle) with estimates of its measurement error as a function of circle radius and as estimated using 6, 12, or 24 sondes (open circles). Variability in $D$ is quantified by the vertical average of the temporal standard deviation of $D$ with height. Error is quantified by vertically averaging the RMSE. In all cases the vertical averaging is over the lower troposphere, defined as the layer between the surface and 5 km.

boundary layer depth—recall the ansatz introduced in the introduction to this manuscript. If this were the case we would expect $\sigma_D$ to be relatively insensitive to $r$ over the mesoscales (20–200 km) that we are exploring. The fact that it is not raises the question of representativeness. How representative is $D$, as measured at a given time and on a given scale, of a "large scale"?

To answer this question we again use the ICON simulations. In this case we compute the divergence profile in the lower 5 km from a circle of a specified size, centered at a specified point at each hour for the last 24 h of a given day's simulation, and we compute the lag correlation of the 24 different divergence estimates. We repeat this analysis for all the days in a particular month and compute the average lag correlation as a function of lag time. The results of this analysis are plotted for two different circle sizes in Fig. 11. The analysis shows that the lag-correlation time scale for $D$ computed over a 100-km circle is about 4 h, and this increases with circle size. A similar analysis is performed for vorticity and vertical velocity (Table 2). It shows that the persistence of $\omega$ follows that of $D$ but that vorticity anomalies are substantially longer lived, increasingly so on larger scales.

ICON simulations further suggest that the divergence on the scale of 200 km, as is measured by a circle of radius 100 km, is reasonably representative of the large scale. Indeed, an isolated boundary layer cloud, with a cloud depth of 1800 m and a mean updraft of $2 \, \text{m s}^{-1}$, defines a time scale of about 15 min, which is much smaller than 4 h.

In addition to looking at how $D$ at a given scale varies with time, we look at how it varies spatially. We do so by
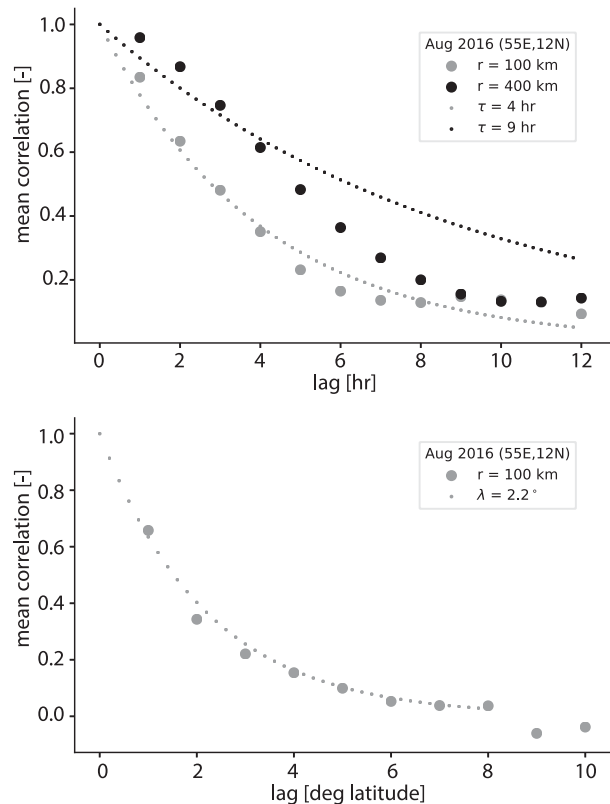


FIG. 11. (a) Time and (b) space autocorrelations of ICON divergence estimates computed for circles of 100- and 400-km radii. The dotted lines represent exponential decay fits to the data.

computing $D$ for circles displaced by 1° longitude along the 12°N latitude line, between 48° and 60°W for a single time (2000 UTC). The spatial lag correlation can then be calculated, and the result, averaged over all days in August, is also shown in Fig. 11. Here the spatial lag correlation is larger than the circle but not by a great deal so that, for a circle of radius 100 km, the spatial lag correlation is about 2.2° or about 225 km, which is hardly larger than the scale of our measurements. Repeating the analysis for the steadier conditions of the winter trades yields similar results except that, at larger ($>6°$) spatial and longer ($>8$ h) time scales, the regressions more closely follow the theoretical curves of Fig. 11 associated with somewhat larger spatial and longer temporal correlations.

For a flow velocity of $7 \, \text{m s}^{-1}$ the advective time scale for a feature of linear dimension of 200 km is about 8 h. This is somewhat larger than the autocorrelation time scale (4 h) identified from the simulations. But even 4 h is much larger than the typical time scale of an individual fair-weather cumulus cloud, whose spatial scale is a few kilometers, and whose temporal scale is a few tens of minutes. Clusters of clouds would have substantially

TABLE 2. Lag-correlation time scales for divergence $D$, vorticity $\zeta$, and pressure velocity $\omega$, as estimated from the analysis of the August 2016 ICON simulations (see text).

| $r$ (km) | $\tau_D (r)$ (h) | $\tau_\zeta (r)$ (h) | $\tau_\omega (r)$ (h) |
|---|---|---|---|
| 25 | 0.7 | 3.2 | 1.2 |
| 50 | 1.9 | 5.6 | 2.5 |
| 100 | 3.9 | 12.9 | 3.8 |
| 200 | 6.6 | 28.4 | 5.5 |
| 400 | 10.2 | 65.2 | 7.6 |

larger space and time scales consistent with the patterning of the larger-scale divergence field, suggesting that $D$ on scales of $O(200)$ km may well influence processes controlling cloudiness on that scale.

## 6. Conclusions and outlook

This paper investigated the possibility of measuring the vertical profile of the divergence of the large-scale horizontal wind, vorticity, and vertical velocity by using dropsondes released from a research aircraft. This possibility was tested during the NARVAL2 airborne field campaign that took place over the western tropical Atlantic in August 2016. Dropsondes were released with high frequency (every 4 min) along circular flight patterns of about 170-km diameter from an altitude of about 9 km. The vertical profile of mass divergence was computed from the horizontal wind profiles as measured from the GPS positioning of the sondes through the course of their descent. The large-scale vertical velocity could then be estimated by integrating the divergence upward from the surface.

By repeating the measurements over pairs of circles flown within the same air mass, it is shown that the divergence and vorticity estimates were amazingly reproducible over a period of about 2 h, consistent with them being indicative of the "large scale" environment rather than measurement noise or small-scale variability in the flow. The close agreement between two different methods for estimating the divergence and vorticity—one that neglects the effects of small-scale variability to provide a regression estimate of an assumed large-scale wind and another that only assumes stationarity in the wind field—further supports the inference that the measured profiles of divergence and vorticity accurately reflect the structure of a well-defined large-scale environment. In addition, it was demonstrated that the estimates from dropsondes are consistent with the observed cloud field, Lagrangian estimates of the large-scale vertical velocity inferred from the spatial structure of the free-tropospheric humidity field, and with simulations from an atmospheric model initialized from meteorological analyses and with a grid scale

a hundredfold finer than the scales of motion being estimated.

Error analyses based both on the sounding data and on the simulation output are also consistent. They suggest that 12 sondes are sufficient to meaningfully measure large-scale (meteorological) variations in $D$, but that useful inferences as to the structure of $D$ may also be possible to derive from as few as 6–8 sondes. Additional analysis of 2 months of simulation output shows that the autocorrelation scales of the divergence in space and time are on the order of 200 km and 4 h, respectively, further supporting the claim that the profile of divergence estimated from dropsonde data is representative of the large-scale environment of shallow clouds.

The observed profiles of divergence exhibited substantial vertical structure and a significant variability on a day-to-day basis and from one region of the trades to the next region. This variability carries over to derived fields such as the large-scale vertical velocity but is also evident in the vorticity. Notwithstanding this considerable variability some common features emerge in the character of the large-scale vertical motion in regimes of suppressed convection. These include maxima around the top of the subcloud layer and around the 0°C isotherm and a minimum near a region of greatly enhanced stability that we identify with the trade-inversion layer (around 2 km).

Although this paper focused on suppressed convective regimes, the technique described here is likely to work in more convective regimes as well. This is illustrated by Fig. 12, which shows the mass divergence and vertical velocity profiles computed from 17 dropsondes released during another circular flight pattern performed in the vicinity of the intertropical convergence zone. In this location, the atmosphere exhibits a large-scale ascent, with a maximum ascent around the top of the subcloud layer (500–600 m above the sea surface) and in the midtroposphere, and a vertical velocity vanishing around 2 km, similar to what was found in more suppressed convective regimes. The ability of the technique to work in deep convective regimes over land remains to be investigated.

The possibility to measure the vertical profiles of large-scale divergence, vorticity, and vertical velocity by using dropsondes deployed from aircraft (or unmanned vehicles) allows atmospheric scientists to meet one of their main observational challenges. One may even predict that these measurements will become routine measurements in future field campaigns and encourage retrospective analysis of dropsonde data from past campaigns. Similar measurements will form a cornerstone of the EUREC[4]A field study, which will take place in the same area as NARVAL2 but during the winter (January–February) 2020. It is hoped that by measuring the large-scale motion field it will be possible to understand the
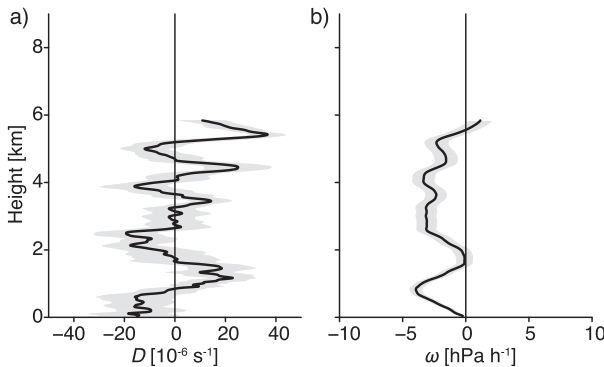
FIG. 12. Vertical profiles of (a) large-scale mass divergence and (b) vertical velocity estimated from 17 dropsondes launched (11 along the first circle and 6 along the second circle) during RF02 on 10 Aug 2016, near the edge of the ITCZ (around 11°N, 49°W, 1700–1800 UTC). Note that HALO flew at FL200 (about 6 km) during this flight.

factors that control shallow cumulus cloud amounts and their coupling to circulations (Bony et al. 2017). Measurements of the large-scale vertical velocity will also make it possible to assess the large-scale tendencies of mass, moisture, and energy that can be used to force models of different types on the one hand, enabling a more critical and quantitative evaluation (through complementary cloud measurements) of their ability to simulate how clouds respond to cloud controlling factors.

Our analysis has focused on establishing the credibility of the measurements. Having done so, however, we cannot resist speculating about some of the physical implications of the observed patterns of divergence and large-scale vertical velocity. In particular the variability of $D$ in both time and space, combined with its rich vertical structure, hints at a closer coupling between the clouds and their environment than is usually presumed. It is usually taken for granted that the large-scale vertical motion and, therefore, the mass divergence field exert a critical influence on clouds. If, in return, the convergence layers noticed in the observations actually constitute "reverberations"—from radiative and condensational processes associated with the clouds and their effects on the humidity field (e.g., Bretherton and Blossey 2017; Stevens et al. 2017)—then this would indeed imply that the interaction between clouds and their environment is very much a two-way coupling. An idea that, at least for the case of shallow convection, suggests a very different view as compared to what is usually adopted in modeling and parameterization studies.

## REFERENCES

Albrecht, B. A., A. K. Betts, W. H. Schubert, and S. K. Cox, 1979: Model of the thermodynamic structure of the trade-wind boundary layer: Part I. Theoretical formulation and sensitivity tests. *J. Atmos. Sci.*, **36**, 73–89, https://doi.org/10.1175/1520-0469(1979)036<0073:MOTTSO>2.0.CO;2.

Alexander, M. J., and J. R. Holton, 2004: On the spectrum of vertically propagating gravity waves generated by a transient heat source. *Atmos. Chem. Phys.*, **4**, 923–932, https://doi.org/10.5194/acp-4-923-2004.

Augstein, E., H. Riehl, F. Ostapoff, and V. Wagner, 1973: Mass and energy transports in an undisturbed Atlantic trade-wind flow. *Mon. Wea. Rev.*, **101**, 101–111, https://doi.org/10.1175/1520-0493(1973)101<0101:MAETIA>2.3.CO;2.

——, H. Schmidt, and F. Ostapoff, 1974: The vertical structure of the atmospheric planetary boundary layer in undisturbed trade winds over the Atlantic Ocean. *Bound.-Layer Meteor.*, **6**, 129–150, https://doi.org/10.1007/BF00232480.

Bannon, J. K., 1949: Large-scale vertical motion in the atmosphere. *Nature*, **163**, 495–496, https://doi.org/10.1038/163495a0.

Bony, S., and Coauthors, 2017: EUREC[4]A: A field campaign to elucidate the couplings between clouds, convection and circulation. *Surv. Geophys.*, **38**, 1529–1568, https://doi.org/10.1007/s10712-017-9428-0.

Bretherton, C. S., and P. N. Blossey, 2017: Understanding mesoscale aggregation of shallow cumulus convection using large-eddy simulation. *J. Adv. Model. Earth Syst.*, **9**, 2798–2821, https://doi.org/10.1002/2017MS000981.

Ciesielski, P. E., W. H. Schubert, and R. H. Johnson, 1999: Large-scale heat and moisture budgets over the ASTEX region. *J. Atmos. Sci.*, **56**, 3241–3261, https://doi.org/10.1175/1520-0469(1999)056<3241:LSHAMB>2.0.CO;2.

Holland, J. Z., 1970: Preliminary report on the BOMEX sea-air interaction program. *Bull. Amer. Meteor. Soc.*, **51**, 809–820, https://doi.org/10.1175/1520-0477(1970)051<0809:PROTBS>2.0.CO;2.

——, and E. M. Rasmusson, 1973: Measurements of the atmospheric mass, energy, and momentum budgets over a 500-kilometer square of tropical ocean. *Mon. Wea. Rev.*, **101**, 44–55, https://doi.org/10.1175/1520-0493(1973)101<0044:MOTAME>2.3.CO;2.

Holton, J. R., J. H. Beres, and X. Zhou, 2002: On the vertical scale of gravity waves excited by localized thermal forcing. *J. Atmos. Sci.*, **59**, 2019–2023, https://doi.org/10.1175/1520-0469(2002)059<2019:OTVSOG>2.0.CO;2.

Johnson, R. H., P. E. Ciesielski, and K. A. Hart, 1996: Tropical inversions near the 0°C level. *J. Atmos. Sci.*, **53**, 1838–1855, https://doi.org/10.1175/1520-0469(1996)053<1838:TINTL>2.0.CO;2.

Klocke, D., B. Brueck, C. Hohenegger, and B. Stevens, 2017: Rediscovery of the doldrums in storm-resolving simulations over the tropical Atlantic. *Nat. Geosci.*, **10**, 891–896, https://doi.org/10.1038/s41561-017-0005-4.

Lenschow, D. H., P. B. Krummel, and S. T. Siems, 1999: Measuring entrainment, divergence, and vorticity on the mesoscale from aircraft. *J. Atmos. Oceanic Technol.*, **16**, 1384–1400, https://doi.org/10.1175/1520-0426(1999)016<1384:MEDAVO>2.0.CO;2.

——, V. Savic-Jovcic, and B. Stevens, 2007: Divergence and vorticity from aircraft air motion measurements. *J. Atmos. Oceanic Technol.*, **24**, 2062–2072, https://doi.org/10.1175/2007JTECHA940.1.

Li, Q., M. Rapp, G. Stober, and R. Latteck, 2018: High-resolution vertical velocities and their power spectrum observed with the MAARSY radar—Part 1: Frequency spectrum. *Ann. Geophys.*, **36**, 577–586, https://doi.org/10.5194/angeo-36-577-2018.

Mapes, B. E., and R. A. Houze Jr., 1995: Diabatic divergence profiles in western Pacific mesoscale convective systems. *J. Atmos. Sci.*, **52**, 1807–1828, https://doi.org/10.1175/1520-0469(1995)052<1807:DDPIWP>2.0.CO;2.

——, P. E. Ciesielski, and R. H. Johnson, 2003: Sampling errors in rawinsonde-array budgets. *J. Atmos. Sci.*, **60**, 2697–2714, https://doi.org/10.1175/1520-0469(2003)060<2697:SEIRB>2.0.CO;2.

Nastrom, G. D., K. S. Gage, and W. H. Jasperson, 1984: Kinetic energy spectrum of large- and mesoscale atmospheric processes. *Nature*, **310**, 36–38, https://doi.org/10.1038/310036a0.

Newell, R. E., 1963: The general circulation of the atmosphere and its effects on the movement of trace substances. *J. Geophys. Res.*, **68**, 3949–3962, https://doi.org/10.1029/JZ068i013p03949.

Nitta, T., and S. Esbensen, 1974: Heat and moisture budget analyses using BOMEX data. *Mon. Wea. Rev.*, **102**, 17–28, https://doi.org/10.1175/1520-0493(1974)102<0017:HAMBAU>2.0.CO;2.

Orlanski, I., 1975: A rational subdivision of scales for atmospheric processes. *Bull. Amer. Meteor. Soc.*, **56**, 527–530.

Romps, D. M., 2012: Weak pressure gradient approximation and its analytical solutions. *J. Atmos. Sci.*, **69**, 2835–2845, https://doi.org/10.1175/JAS-D-11-0336.1.

Sobel, A. H., and C. S. Bretherton, 2000: Modeling tropical precipitation in a single column. *J. Climate*, **13**, 4378–4392, https://doi.org/10.1175/1520-0442(2000)013<4378:MTPIAS>2.0.CO;2.

Stevens, B., and Coauthors, 2016: The Barbados Cloud Observatory: Anchoring investigations of clouds and circulation on the edge of the ITCZ. *Bull. Amer. Meteor. Soc.*, **97**, 787–801, https://doi.org/10.1175/BAMS-D-14-00247.1.

——, H. Brogniez, C. Kiemle, J.-L. Lacour, C. Crevoisier, and J. Kiliani, 2017: Structure and dynamical influence of water vapor in the lower tropical troposphere. *Surv. Geophys.*, **38**, 1371–1397, https://doi.org/10.1007/s10712-017-9420-8.

van der Dussen, J. J., S. R. de Roode, and A. P. Siebesma, 2016: How large-scale subsidence affects stratocumulus transitions. *Atmos. Chem. Phys.*, **16**, 691–701, https://doi.org/10.5194/acp-16-691-2016.

Wang, J. J., and Coauthors, 2015: A long-term, high-quality, high-vertical-resolution GPS dropsonde dataset for hurricane and other studies. *Bull. Amer. Meteor. Soc.*, **96**, 961–973, https://doi.org/10.1175/BAMS-D-13-00203.1.

Yanai, M., S. Esbensen, and J.-H. Chu, 1973: Determination of bulk properties of tropical cloud clusters from large-scale heat and moisture budgets. *J. Atmos. Sci.*, **30**, 611–627, https://doi.org/10.1175/1520-0469(1973)030<0611:DOBPOT>2.0.CO;2.